Nanoscale Horizons

ROYAL SOCIETY OF CHEMISTRY

COMMUNICATION

View Article Online
View Journal | View Issue



Cite this: *Nanoscale Horiz.*, 2023, 8, 211

Received 29th September 2022,
Accepted 28th November 2022

DOI: 10.1039/d2nh00451h

rsc.li/nanoscale-horizons



# Theoretical exploration of the nitrogen fixation mechanism of two-dimensional dual-metal $TM_1TM_2@C_9N_4$ electrocatalysts†

Jinxin Sun,‡[a] Peng Xia,‡[a] Yuxing Lin,‡[a] Yunfan Zhang,[a] Anjie Chen,[a] Li Shi,[b] Yongjun Liu,[a] Xianghong Niu, *[c] Ailei He*[a] and Xiuyun Zhang *[a]

**The electrochemical nitrogen reduction reaction (eNRR) to $NH_3$ has become an alternative to traditional $NH_3$ production techniques, while developing NRR catalysts with high activity and high selectivity is of great importance. In this study, we systematically investigated the potentiality of dual transition metal (TM) atom anchored electrocatalysts, $TM_1TM_2@C_9N_4$ ($TM_1$, $TM_2$ = 3(4)d TM atoms), for the NRR through the first principles high-throughput screening method. A total of 78 $TM_1TM_2@C_9N_4$ candidates were designed to evaluate their stability, catalytic activity, and selectivity for the NRR. Four $TM_1TM_2@C_9N_4$ candidates ($TM_1TM_2$ = NiRu, FeNi, TiNi, and NiZr) with an end-on $N_2$ adsorption configuration, and two candidates ($TM_1TM_2$ = TiNi and TiFe) with a side-on adsorption configuration, were screened out with the advantage of suppressing the hydrogen evolution reaction (HER) and exhibiting high NRR activity. Moreover, the catalysts with end-on and side-on $N_2$ adsorption configurations were determined to favor distal and consecutive reaction pathways, respectively, with favorable limiting potentials of only −0.33 V to −0.53 V. Detailed analysis showed that the $N_2$ adsorption and activation are primarily ascribed to the strong back-donation interactions between the d-electrons of TM atoms and the anti-orbitals of an $N_2$ molecule. Our findings pave a way for the rational design and rapid screening of highly active $C_9N_4$-based catalysts for the NRR.**

### New concepts

Inspired by the synergistic effect of multi-active centers in dual-atom catalysts (DACs) or few-atom catalysts (FACs), we proposed to explore the nitrogen reduction reaction (NRR) performance of $TM_1TM_2@C_9N_4$ (TM = 3(4)d transition metal atoms) electrocatalysts by a high-throughput screening method. Compared with many SACs and DACs, the screened dual-metal atom $TM_1TM_2@C_9N_4$ candidates are found to display ultra-high stabilities, high NRR activity, and ability to effectively suppress the hydrogen evolution reaction (HER). The superior activity of these $TM_1TM_2@C_9N_4$s can primarily be ascribed to the strong back-donation interactions between the d-electrons of TM atoms and the anti-orbitals of a $N_2$ molecule and other nitrogen intermediates. This study paves a way for the rational design and rapid screening of highly active $C_9N_4$-based catalysts for the NRR.

## 1. Introduction

Currently, the electrochemical nitrogen reduction reaction (eNRR) to ammonia ($NH_3$) is attracting more attention due to its mild conditions with attractive features of low cost and sustainable development,[1–3] and is regarded as one promising way to break the barrier of industrial $NH_3$ synthesis under harsh conditions. During the eNRR, the use of suitable catalysts is crucial, because the inertness of $N_2$ leads to the difficulty of its adsorption and activation, leading to a low reaction efficiency.[4–6] In addition, the $N_2$ reduction process is seriously suppressed by the accompanying hydrogen evolution reaction (HER).[7–9] Therefore, designing or fabricating NRR catalysts with high activity and high selectivity is one great challenge for researchers.

To date, various electrocatalysts for the NRR have been developed and explored by experimental and theoretical researchers.[10–13] Among them, the single-metal atom catalysts (SACs) or few-metal atom catalysts (FACs), in which single or few metal atoms are well adsorbed on suitable substrates, are becoming one promising type of candidates for the eNRR and other electrochemical reactions due to their advantage of precisely controlling the rate-determining or other reaction steps.[14–17] For example, Zeng *et al.* synthesized a N-doped carbon monolayer with Ru atoms anchored, which

[a] College of Physics Science and Technology, Yangzhou University, Yangzhou 225002, China. E-mail: heailei@yzu.edu.cn, xyzhang@yzu.edu.cn
[b] State Key Laboratory of Organic Electronics and Information Displays & Institute of Advanced Materials (IAM), Jiangsu National Synergetic Innovation Center for Advanced Materials (SICAM), School of Materials Science and Engineering, Nanjing University of Posts and Telecommunications, Nanjing 210023, China
[c] New Energy Technology Engineering Laboratory of Jiangsu Province & School of Science, Nanjing University of Posts and Telecommunications, Nanjing, 210023, China. E-mail: xhniu@njupt.edu.cn

† Electronic supplementary information (ESI) available. See DOI: https://doi.org/10.1039/d2nh00451h

‡ Jinxin Sun, Peng Xia, and Yuxing Lin contributed equally to this work.

achieved a record-high faradaic efficiency (FE) of 29.6% and a yield rate of 120.9 $\mu g_{NH_3}$ $h^{-1}$ $mag_{cat}^{-1}$.[18] Li *et al.* reported that the SAC of Mo atoms atomically distributed graphdiyne and has a high FE of over 21% and a yield rate of 145.4 $\mu g_{NH_3}$ $h^{-1}$ $mag_{cat}^{-1}$.[19] However, the key challenge in designing outstanding SACs or FACs is the choice of supporting substrates, which play an important role in anchoring and transferring charges to metal atoms. Interestingly, various 2D materials, *e.g.*, graphene,[20] transition metal dichalcogenides (TMDs),[21,22] hexagonal BN,[23] *etc.*, have been widely used as supports for SACs or FACs. Particularly, B or N atom doped 2D materials are confirmed to be good at binding and enhancing the catalytic activity of metal atoms.[24–26] Through density functional theory calculations, Le *et al.* revealed that SACs obtained by Mo anchoring on N-doped graphene can achieve 100% selectivity for $N_2$ fixation.[27] Similarly, Zhao *et al.* found that "$CrN_3$" doped graphene possesses excellent catalytic performance for $N_2$ reduction.[28] Interestingly, Jiao *et al.* revealed that the NRR activity of the Fe atom in Fe–N–C SACs can be greatly improved by coordinating with a B dopant,[29] in which the limiting potential ($U_L$) of the NRR on Fe–$B_2N_2$ is −0.65 V. Besides, Ou *et al.* found a highly active NRR catalyst by embedding isolated Mo atoms on N-doped black phosphorous,[30] with $U_L$ of −0.56 V.

In addition to SACs, the FACs possessing two or more active metal centers[31,32] were also revealed to be potential NRR catalysts due to their synergistic effects in adjusting the adsorption configuration of NRR reactive species and reducing the energy barrier in the reaction process. For example, Luo *et al.* reported that the FeMo dual atomic cluster embedded on N-doped carbon shows an FE of 41.7% at 0.2 V for the NRR, much smaller than those of its SAC counterparts ($FeN_4$ and $MoN_4$).[33] Deng *ET AL.* systematically studied the NRR reactivity of homo dual atomic catalysts formed by 20 transition metal (TM) elements supported by N-doped graphene and screened out $Ru_2N_6$@G as an excellent catalyst.[34] Zheng *et al.* theoretically designed hetero dual-metal Fe/M–N–C catalysts and revealed the synergistic effect of Fe/M dual-metal active sites by theoretical calculations.[35] Very recently, Zheng *et al.* systematically investigated the catalytic performance of various triple-TM clusters anchored on nitrogen-doped graphene for the NRR and confirmed that $Co_3$–$N_4$@G possesses the highest activity with a limiting potential of −0.41 V through the enzymatic mechanism.[36] Moreover, Li and co-workers revealed that $Ru_3$–$N_4$@G with three Ru trimer clusters anchored on N-doped carbon ($Ru_3$–$N_4$) have better 2-amino-benzaldehyde catalytic activity than the SAC counterpart of $RuN_4$.[37]

Furthermore, many pristine 2D $C_xN_y$ systems, such as g-$C_3N_4$, g-$C_2N$, and g-CN, have received extensive attention in many catalysis fields due to their large surface area, high stability, rich coordination environments, *etc.*[16,38,39] As a member of the $C_xN_y$ family, $C_9N_4$ possesses semimetallic properties, high thermodynamic stability, and numerous nanopores favorable for TM loading.[40] For example, Zhou *et al.* theoretically designed Ni@$C_9N_4$ bifunctional electrocatalysts for efficient water splitting.[41] Chen *et al.* screened TM@$C_9N_4$ (TM = 3d, 4d, and 5d TM atoms) candidates for potential NRR catalysts by high-throughput computation, and found that the optimal catalyst W@$C_9N_4$ favors the distal mechanism with a confinement potential of −0.24 V.[42] However, the work of anchoring homo-/hetero-nuclear transition metal atoms on $C_9N_4$ to obtain excellent NRR catalysts has not been addressed.

In this work, we systematically explored the NRR performance of bimetal catalysts, $TM_1TM_2$@$C_9N_4$ ($TM_1TM_2$ = 3d, 4d TM atoms), by first principles high-throughput calculations. A total of 78 $TM_1TM_2$@$C_9N_4$ candidates, including 12 homo dual TM based systems and 66 hetero dual TM based systems, are considered. After the six-step screening, we obtained five high activity $TM_1TM_2$@$C_9N_4$ catalysts with high stability and high selectivity.

## 2. Computational methods and modeling

All the calculations were carried out using the projector augmented wave (PAW) method as implemented in the Vienna *ab initio* simulation package (VASP).[43,44] The exchange–correlation interaction was treated using the generalized gradient approximation (GGA) parameterized by Perdew,[45] Burke and Ernzerhof (PBE).[46,47] A vacuum space of 18 Å was inserted in the *z*-direction of the 2 × 2 × 1 $C_9N_4$ supercell to eliminate the interaction between adjacent periodic units. 3 × 3 × 1 Monkhorst–Pack *k*-point meshes were applied to sample the first Brillouin zone, while denser *k*-points of 7 × 7 × 1 were applied for electronic structure calculations. In structural relaxation, the total energy and the force on each relaxed atom were converged to $10^{-5}$ eV and 0.01 eV $Å^{-1}$. Spin polarization is considered, and the energy cutoff for the plane-wave basis set was 450 eV. *Ab initio* molecular dynamics (AIMD) simulations were applied to identify the thermodynamic stability of $TM_1TM_2$@$C_9N_4$ candidates.[48] In the electrochemical process of the NRR, six proton and electron transfer steps, *e.g.*, $N_2 + 6H^+ + 6e^- \rightarrow 2NH_3$, are evolved. To efficiently evaluate the NRR activity of all the $TM_1TM_2$@$C_9N_4$ candidates, the reaction free energy ($\Delta G$) for each fundamental step was calculated according to the computational hydrogen electrode (CHE) model.[49,50] In this framework, the chemical potential of the proton–electron pair ($H^+ + e^-$) can be referenced to one half of that of $H_2$ under standard reaction conditions, and the change in the reaction free energy for each step can be evaluated as:

$$\Delta G = \Delta E + \Delta ZPE - T\Delta S + eU + \Delta G_{pH} \quad (1)$$

where $\Delta E$, $\Delta ZPE$, $T$, and $\Delta S$ are the reaction energy, zero-point energy, temperature (298.15 K), and entropy change, respectively. $eU$ is the free energy contribution related to the applied potential $U$. $\Delta G_{pH}$ is the free energy correction of pH, which is the free energy correction related to $H^+$ concentration and can be calculated using $\Delta G_{pH} = k_B T \times pH \times \ln 10$, and the pH value is assumed to be 0.

 

# 3. Results and discussion

### 3.1. Structures and stability of $TM_1TM_2@C_9N_4$

First, we investigated the structures and stabilities of these $TM_1TM_2@C_9N_4$ catalysts. As shown in Fig. 1a and b, the selected substrate is a 2 × 2 $C_9N_4$ supercell containing 72 carbon atoms and 32 nitrogen atoms. Here, eight of the 3d TM atoms (*e.g.*, Ti, V, Cr, Mn, Fe, Co, Ni, and Cu) and four of the 4d TM atoms (*e.g.*, Zr, Mo, Tc, and Ru) were taken into consideration. As a result, 78 dual-metal $TM_1TM_2@C_9N_4$ catalysts were constructed, including 12 homonuclear and 66 heteronuclear systems. Besides, three types of anchoring sites ($S_1$, $S_2$, and $S_3$) were tested: (i) $S_1$ configuration, two TM atoms sit in a horizontal line with each atom binding to three adjacent N atoms (see Fig. 1a), (ii) $S_2$ configuration, the TM–TM bond of the S1 configuration was anticlockwise rotated by 30 degree (see Fig. 1b), in which each TM atom only bonds with two nearest N atoms, and (iii) $S_3$ configuration, two TM atoms from the systems are no longer coordinated equally, and bind with two and three adjacent N atoms, respectively (see Fig. 1c). All the optimized structures are shown in Fig. S1–S4 in the ESI.† Clearly, no significant structural deformation is found for all the studied $TM_1TM_2@C_9N_4$ systems. For $TM_1TM_2@C_9N_4$ anchored with homonuclear dual-metal atoms ($TM_1$ = $TM_2$, see Fig. S1, ESI†), the $S_1$ configuration is favored for those with smaller diameters, *e.g.*, Fe, Co, and Ni, and the $S_2$ configuration is preferred for the candidates having larger diameters, *e.g.*, Ti–Mn, Cu, Zr, and Ru. Similarly, for $TM_1TM_2@C_9N_4$ combined with hetero TM atoms ($TM_1 \neq TM_2$), the $S_1$ configuration is observed for those with close to TM diameters (see Fig. S2, ESI†), and the $S_2$ one is found for those with larger TM diameters (see Fig. S3, ESI†). And for the systems with large diameter differences for two TM atoms, taking

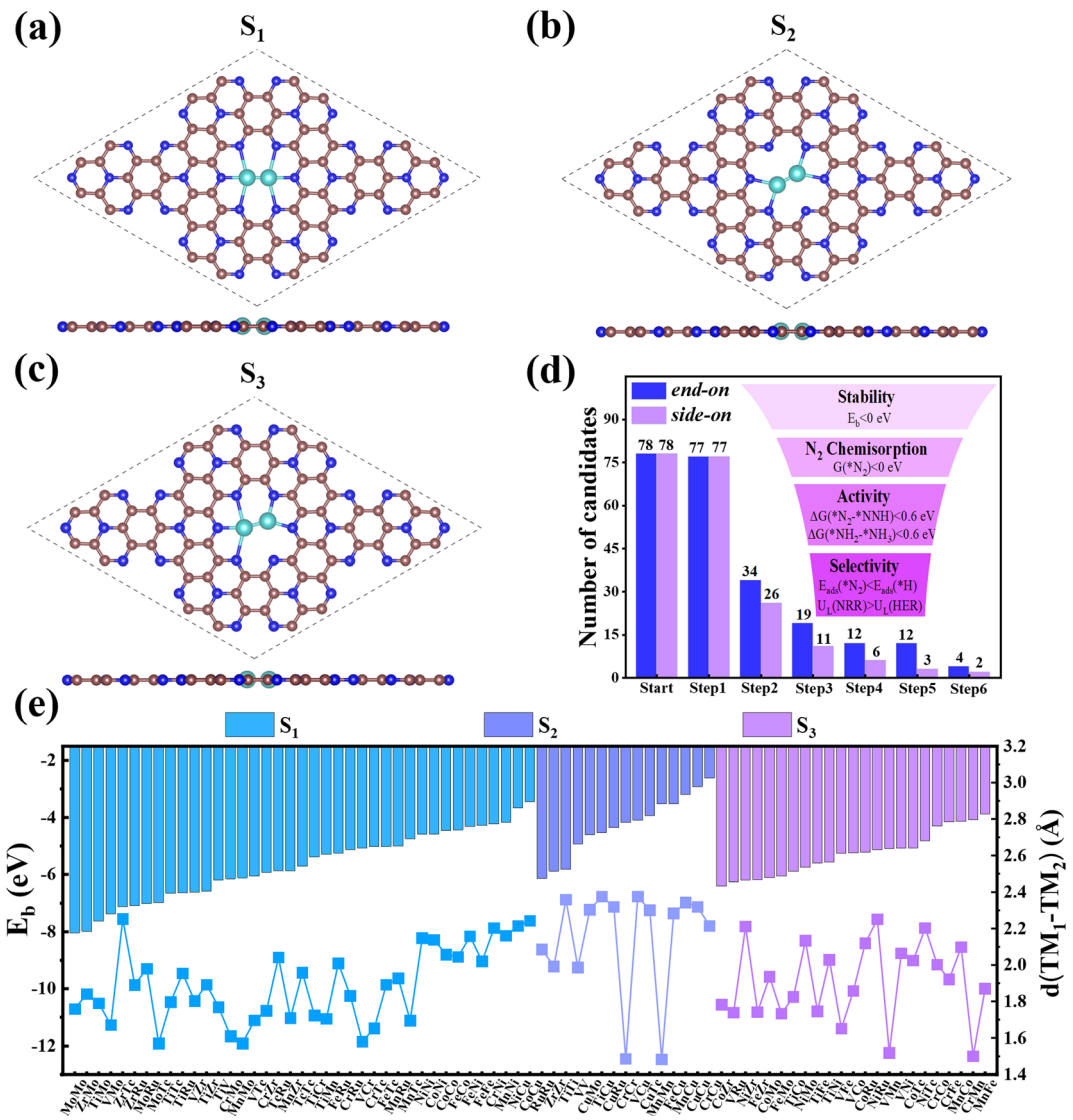


Fig. 1 Top and side views of (a) $S_1$-, (b) $S_2$- and (c) $S_3$-configuration $TM_1TM_2@C_9N_4$. (d) Schematic illustration of the screening results by the "six-step" strategy. (e) Binding energies of dual TM atoms ($TM_1$ and $TM_2$) ($E_b$) and $TM_1$–$TM_2$ bond length ($d_{TM1-TM2}$) of the 78 $TM_1TM_2@C_9N_4$ catalysts. The brown, navy blue and light blue balls represent C, N, and TM atoms, respectively.

CuTM@$C_9N_4$s (TM = Ti, V, Cr, Mn, Fe, Ru, Mo, and Tc) as an example, the Cu atom with a large atomic diameter favors the $S_2$ bonding style, while the other TM atoms with smaller diameters favor the $S_3$ bonding style. As the Cu atom sits out of the CuZr@$C_9N_4$ plane, it is unsuitable to form a dual catalytic center site for nitrogen adsorption. The $TM_1$–$TM_2$ bond lengths ($d_{TM1-TM2}$) of the remaining systems are around 1.484–2.376 Å, which are smaller than those in their metal bulk (see Fig. 1e). Among which, $Mn_2$@$C_9N_4$ has the shortest $d_{TM1-TM2}$ (= 1.484 Å), while TiCu@$C_9N_4$ has the longest $d_{TM1-TM2}$ (= 2.376 Å).

To explore the stability of these $TM_1TM_2$@$C_9N_4$ systems, we calculated their binding energies ($E_b$) per TM atom using the following equation:

$$E_b = \frac{E_{TM_1TM_2@C_9N_4} - E_{C_9N_4} - E_{TM_1} - E_{TM_2}}{2} \quad (2)$$

where $E_{TM_1TM_2@C_9N_4}$ and $E_{C_9N_4}$ are the energies of the $TM_1TM_2$@$C_9N_4$ monolayer and the $C_9N_4$ monolayer. $E_{TM_1}$ and $E_{TM_2}$ represent the energies of the isolated TM atoms. As Fig. 1e illustrates, the binding energies of all the studied $TM_1TM_2$@$C_9N_4$ systems are in the range from −8.64 eV to −2.62 eV, close to those of the TM@$C_9N_4$ monolayer and other carbon-based substrates doped with single or double TM atoms. The negative binding energies ($E_b < 0$) indicate the strong interaction of TM atoms on the $C_9N_4$ substrate, which is also the first step of screening criteria for suitable NRR catalysts. Such $E_b$ is in line with the structural characters, as shown in Fig. 1c, and the candidates with smaller $d_{TM1-TM2}$ are found to have more prominent binding energies, and *vice versa*.

### 3.2. $N_2$ adsorption and activation of $TM_1TM_2$@$C_9N_4$

Then, we systematically explored the adsorption of $N_2$, which is the prerequisite for the subsequent hydrogenation process in the NRR. Generally, two forms of $N_2$ adsorption on catalysts, end-on and side-on configurations, are considered. In the two dual-metal atom doped systems, we investigated six possible adsorption ways, including two end-on adsorption configurations (E-1 and E-2, see Fig. 2a and b) and four side-on adsorption configurations (S-1, S-2, S-3, and S-4, see Fig. 2c–f). For the E-1 configuration, the end N atom from $N_2$ sits atop one TM atom (see Fig. 2a), while for the E-2 configuration, the end N atom from $N_2$ resides on the bridge site of two TM atoms (see Fig. 2b). As for S configurations, the $N_2$ plane is parallel with the $C_9N_4$ substrate. Of these, the S-1 and S-4 configurations have structures with the N≡N bond perpendicular to the TM–TM bond (see Fig. 2c and f), while for S-2 and S-3 configurations, the N≡N bond is found to be parallel to the TM–TM bond (see Fig. 2d and e).

In order to ensure the effective adsorption of $N_2$, the Gibbs free energy of $N_2$, $\Delta G(*N_2) < 0$ eV, is set as the second screening criterion, and the catalysts that could effectively adsorb $N_2$ in two adsorption configurations are selected. The $\Delta G(*N_2)$ values of 77 $TM_1TM_2$@$C_9N_4$ with end-on and side-on bonding characters are described in Fig. 2g and h, respectively. It is observed that $\Delta G(*N_2)$ values on 34 $TM_1TM_2$@$C_9N_4$ with end-on adsorption for $N_2$ are negative, ranging from −0.001 to −0.91 eV. Besides, 26 candidates with side-on adsorption for $N_2$ are confirmed to have negative $\Delta G(*N_2)$, around −0.03 to −1.60 eV. Among which, 17 systems display negative $\Delta G(*N_2)$ in both adsorption configurations, ranging from −0.03 to −0.85 eV. Except TiNi@$C_9N_4$, TiCu@$C_9N_4$, and FeNi@$C_9N_4$, the $\Delta G(*N_2)$ values of all the other $TM_1TM_2$@$C_9N_4$ candidates with end-on adsorption patterns are more negative than those of side-on configurations, indicating that they are more energetically favorable. It is noted that most candidates containing Cr or Mn atoms (20 systems) are not conducive to the adsorption of $N_2$; exceptions are found for CrNi@$C_9N_4$, CrCu@$C_9N_4$, and MnCu@$C_9N_4$ candidates with side-on adsorption configurations. The inertness of these candidates can be ascribed to the stable half occupied electronic structures of Cr($3d^5 4s^1$) or Mn($3d^5 4s^2$). As for the systems containing 4d TM (= Zr, Mo, Tc, and Ru) atoms, end on adsorption of $N_2$ is favored, with an exception of TiZr@$C_9N_4$.

The N≡N bond lengths ($d_{N\equiv N}$) of the adsorbed $N_2$ molecule on these $TM_1TM_2$@$C_9N_4$ candidates are summarized in Fig. 2g and h. Compared with the free $N_2$ molecule (1.12 Å), the N≡N bond lengths for $*N_2$ were elongated, indicating the effective activation of the $N_2$ molecule. For the end-on adsorbed systems, the $d_{N\equiv N}$ values (= 1.147Å–1.160 Å) of the E-2 adsorption configurations are longer than those of the E-1 ones ($d_{N\equiv N}$ = 1.120–1.148 Å) (see Fig. 2g). However, for the side-on adsorbed systems, the $d_{N\equiv N}$ of $*N_2$ is much longer, around 1.162–1.279 Å, indicating that the $N_2$ molecule is more pronouncedly activated. Moreover, the $d_{N\equiv N}$ of the systems with the S-1 adsorption configuration (1.221–1.299 Å) is longer than those of the other three adsorption configurations (S-2: 1.167–1.247 Å, S-3: 1.162–1.187 Å, and S-4: 1.169–1.204 Å).

To explain the origin of the activation of $N_2$ on these $TM_1TM_2$@$C_9N_4$ substrates, the relationships of the N≡N bond length ($d_{N\equiv N}$) and the charge transfer from the $TM_1TM_2$@$C_9N_4$ substrate to $*N_2$ ($\Delta Q$) are summarized in Fig. 2g and h. Clearly, the $d_{N\equiv N}$ is linearly related to $\Delta Q$ from $TM_1TM_2$@$C_9N_4$ to $*N_2$; that is, the more the charge transfer, the longer the N≡N bond length. Compared with the systems with end-on configurations ($\Delta Q$ = 0.096–0.489 *e*), more charge transfer is found for the ones with side-on configurations, *e.g.*, $\Delta Q$ = 0.327–1.071 *e* (see Fig. 2g and h). Accordingly, $d_{N\equiv N}$ values of the $*N_2$ in the side-on adsorption systems are longer than those of the end-on ones as discussed above. Also, the significant difference between $d_{N\equiv N}$ and $\Delta Q$ indicates that $TM_1TM_2$@$C_9N_4$ systems with side-on configurations for $N_2$ are easier to obtain electrons and activate the N≡N triple bond. Moreover, the systems with the E-2 adsorption configuration have more charge transfer ($\Delta Q$ = 0.333–0.489 *e*) than those of the E-1 adsorption configuration ($\Delta Q$ = 0.096–0.399 *e*), indicating that the E-2 adsorption configuration is easier to activate $N_2$ than the E-1 ones. The different activation behaviors can be attributed to the direct interaction between the N atoms of the E-2 adsorption configuration and the two TM atoms. As shown in Fig. 2j, the $\Delta Q$ of the S-1 adsorption configurations ($\Delta Q$ = 0.626–1.071 *e*) is higher than those of the S-3 ($\Delta Q$ = 0.327–0.496 *e*) and S-4 ($\Delta Q$ = 0.359–0.569 *e*) ones, indicating that the S-1 adsorption configuration is more likely to activate $N_2$, which can be attributed to the direct interaction of both N atoms with TM atoms in the S-1

 

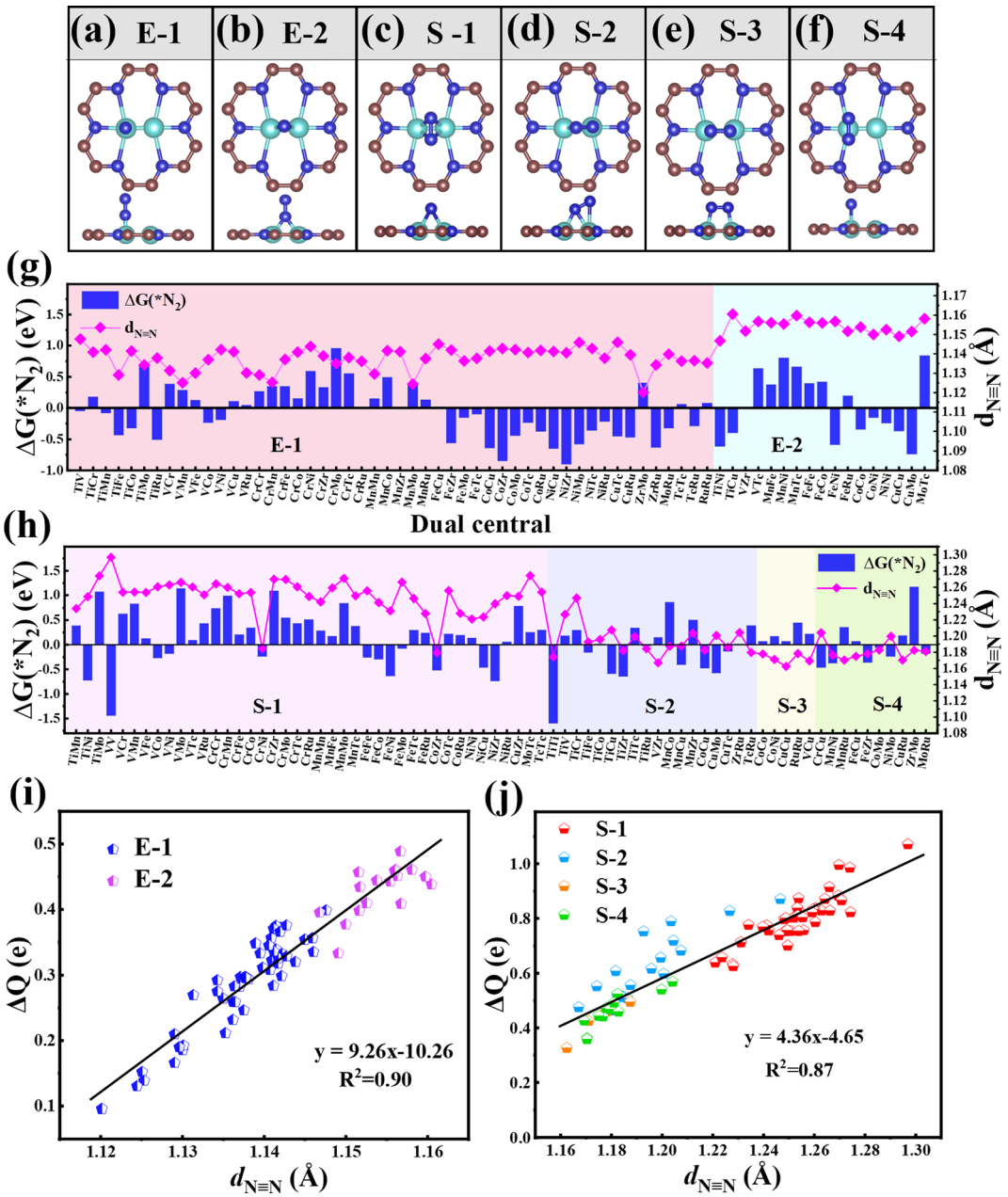


Fig. 2 The considered adsorption configurations of (a and b) end-on (E-1, E-2) and (c–f) side-on (S-1, S-2, S-3, and S-4) for $N_2$ on the $TM_1TM_2@C_9N_4$ substrate. Gibbs free energy change $G(*N_2)$ values and N≡N bond lengths of $*N_2$ ($d_{N\equiv N}$) adsorbed on 77 $TM_1TM_2@C_9N_4$ catalysts with (g) end-on and (h) side-on adsorption configurations. Relationships between charge transfer ($\Delta Q$) and $d_{N\equiv N}$ adsorbed on 77 $TM_1TM_2@C_9N_4$ catalysts through (i) end-on and (j) side-on adsorption configurations.

adsorption configuration. In contrast, the $\Delta Q$ of the S-2 adsorption configuration is moderate due to the direct interaction of one N with two TM atoms and the other N with only one TM atom. Based on the above analysis, we considered 34 $TM_1TM_2@C_9N_4$ candidates with the end-on configuration and 26 candidates with the side-on configuration having $\Delta G(*N_2) < 0$ eV in the following section (see Fig. 1d).

### 3.3. The NRR process of $TM_1TM_2@C_9N_4$

As the catalytic efficiency of the NRR is usually limited by the first and last protonation steps,[39,42] the free energy change of the first and last hydrogenation steps is set to be less than 0.60 eV, that is $\Delta G_{*N_2 \rightarrow *NNH} < 0.60$ eV, $\Delta G_{*NH_2 \rightarrow *NH_3} < 0.60$ eV, as the third and fourth step screening criteria.[52] Fig. 3a and b plot the Gibbs free energy changes of the first ($\Delta G_{*N_2 \rightarrow *NNH}$) and last ($\Delta G_{*NH_2 \rightarrow *NH_3}$) protonation steps of the candidates with end-on and side-on $N_2$ adsorption configurations. As shown in Fig. 3a, 15 candidates with the end-on adsorption configuration like $CoRu@C_9N_4$, $CuTc@C_9N_4$, *etc.* are eliminated due to their larger protonation energy of $\Delta G_{*N_2 \rightarrow *NNH} > 0.6$ eV, leaving the remaining 19 candidates for potential catalysts. Next, 7 candidates, like $VZr@C_9N_4$, $TiV@C_9N_4$, *etc.*, are further

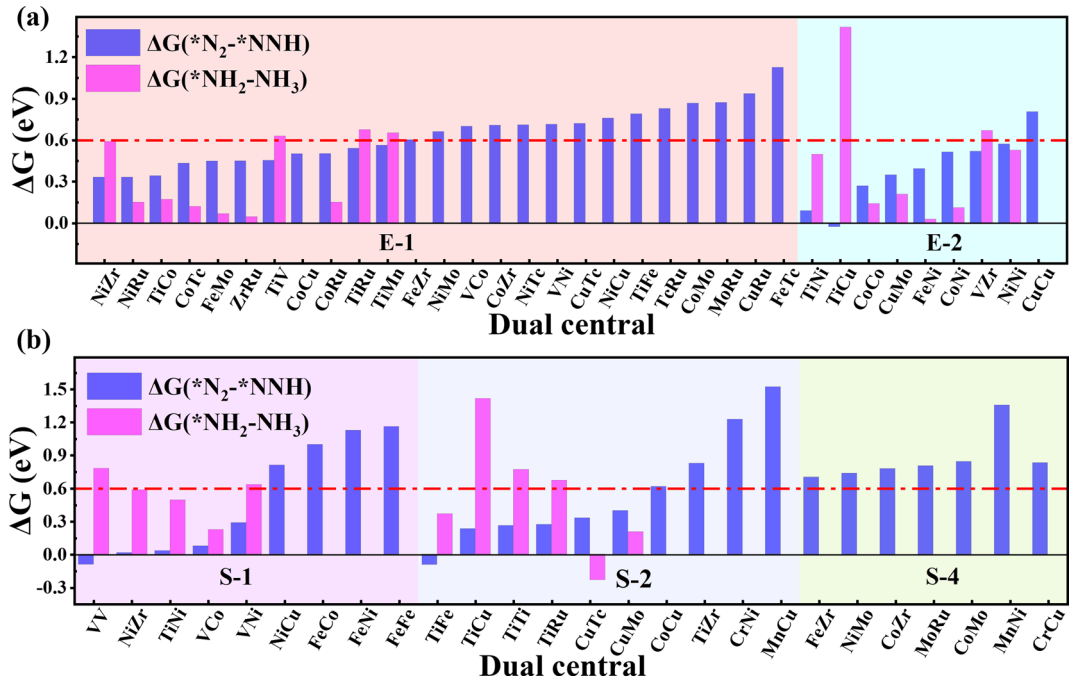


Fig. 3 Gibbs free energy change of $*N_2 + H^+ + e^- \rightarrow *NNH$ ($\Delta G(*N_2{-}*NNH)$) and $*NH_2 + H^+ + e^- \rightarrow *NH_3$ ($\Delta G(*NH_2{-}*NH_3)$) adsorbed on 34 and 26 $TM_1TM_2@C_9N_4$ catalysts through (a) end-on and (b) side-on configurations.

rejected due to their higher protonation energies in the last step with $\Delta G_{*NH_2 \rightarrow *NH_3} > 0.6$ eV. For the side-on adsorption configurations, respective 15 candidates and 5 candidates are rejected due to the higher energies for the first and last protonation steps (see Fig. 3b). As a result, 18 $TM_1TM_2@C_9N_4$ candidates with 12 end-on and 6 side-on adsorption configurations are reserved based on the third and fourth step screening criteria (see Fig. 1d).

To carefully examine the potential-determining step (PDS) of each catalyst, we further do a full reaction path search for the remaining 18 $TM_1TM_2@C_9N_4$ candidates. For 12 end-on adsorption configurations, 8 $TM_1TM_2@C_9N_4$ candidates ($TM_1TM_2$ = NiRu, TiCo, CoTc, FeMo, CoRu, NiTc, NiZr, and CoCo) with E-1 $N_2$ adsorption configurations and 4 $TM_1TM_2@C_9N_4$ candidates ($TM_1TM_2$ = FeNi, TiNi, CoNi, and NiNi) with E-2 $N_2$ adsorption configurations are determined. As for 6 side-on adsorption candidates, respective 3 $TM_1TM_2@C_9N_4$ candidates ($TM_1TM_2$ = VCo, TiNi, and NiZr) with S-1 adsorption configurations and 3 S-2 candidates ($TM_1TM_2$ = CuTc, TiFe, and CuMo) are determined. As shown in Scheme 1, various NRR reaction pathways of different $N_2$ adsorption configurations are discussed. For the candidates with the end-on adsorption configuration, distal and alternating paths are considered, respectively. And for the systems with the side-on adsorption configuration, consecutive and enzymatic paths are considered. For the alternating and enzymatic paths, proton–electron pairs are added alternately to the two N atoms, while for the distal and consecutive paths, the proton–electron pairs continuously attack the same one of two N atoms until the first $NH_3$ is released.

The limiting potential ($U_L$), the lowest negative voltage endows a spontaneous hydrogenation reaction, can also be used to reveal the activity of NRR electrocatalysts. The $U_L$ of

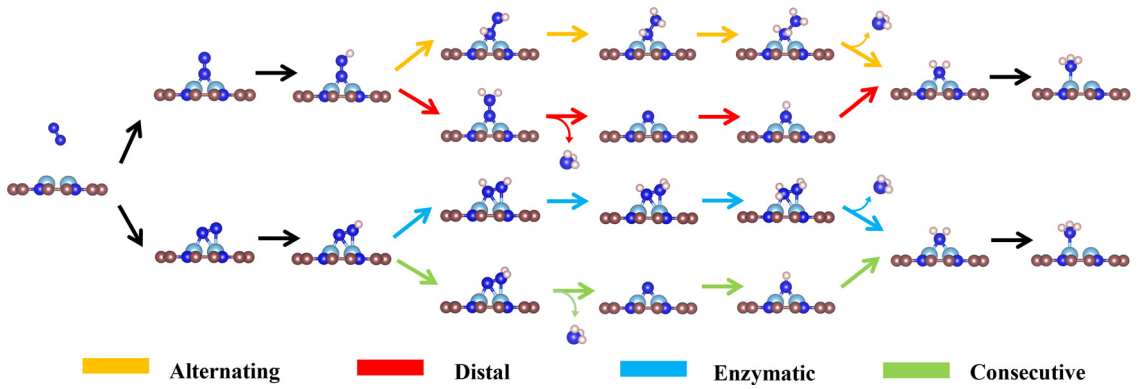


Scheme 1 Schematic diagram of possible reaction pathways for the NRR on $TM_1TM_2@C_9N_4$.

 

the NRR can be calculated using the following equation:

$$U_L = -\frac{\Delta G}{e} \quad (3)$$

where $\Delta G$ refers to the free energy difference of the PDS under various reaction pathways. Fig. 4a illustrates the $U_L$s of the 18 remaining $TM_1TM_2@C_9N_4$ candidates.

Our results show that all the studied candidates are more active than the Ru(0001) stepped surface with smaller $U_L$s ($<-1.0$ V).[38] Particularly, four candidates $Co_2@C_9N_4$ ($U_L = -0.27$ V), $NiRu@C_9N_4$ ($U_L = -0.33$ V), $TiCo@C_9N_4$ ($U_L = -0.34$ V), and $FeNi@C_9N_4$ ($U_L = -0.35$ V) are determined to be potentially excellent catalysts with high activity. The relationship between the catalyst activity and intrinsic properties is important for understanding the origin of catalytic activity and guiding the rational design of catalysts. According to the Sabatier principle,[51] moderate binding between the catalyst surface and reaction intermediates will provide an optimal catalyst. Fig. 4b shows the volcano curve between $U_L$s and adsorption energy for the $N_2$ molecule ($\Delta E_{ads}(*N_2)$) of the potentially highly active catalysts with the end-on configuration of $N_2$. Among all the candidate catalysts, $Co_2@C_9N_4$ is the closest to the top of the volcano plot, which has a moderate ($\Delta E_{ads}(*N_2) = -0.81$ eV) $N_2$ adsorption binding and the highest catalytic activity. If the adsorption strength of $N_2$ is too strong or too weak,

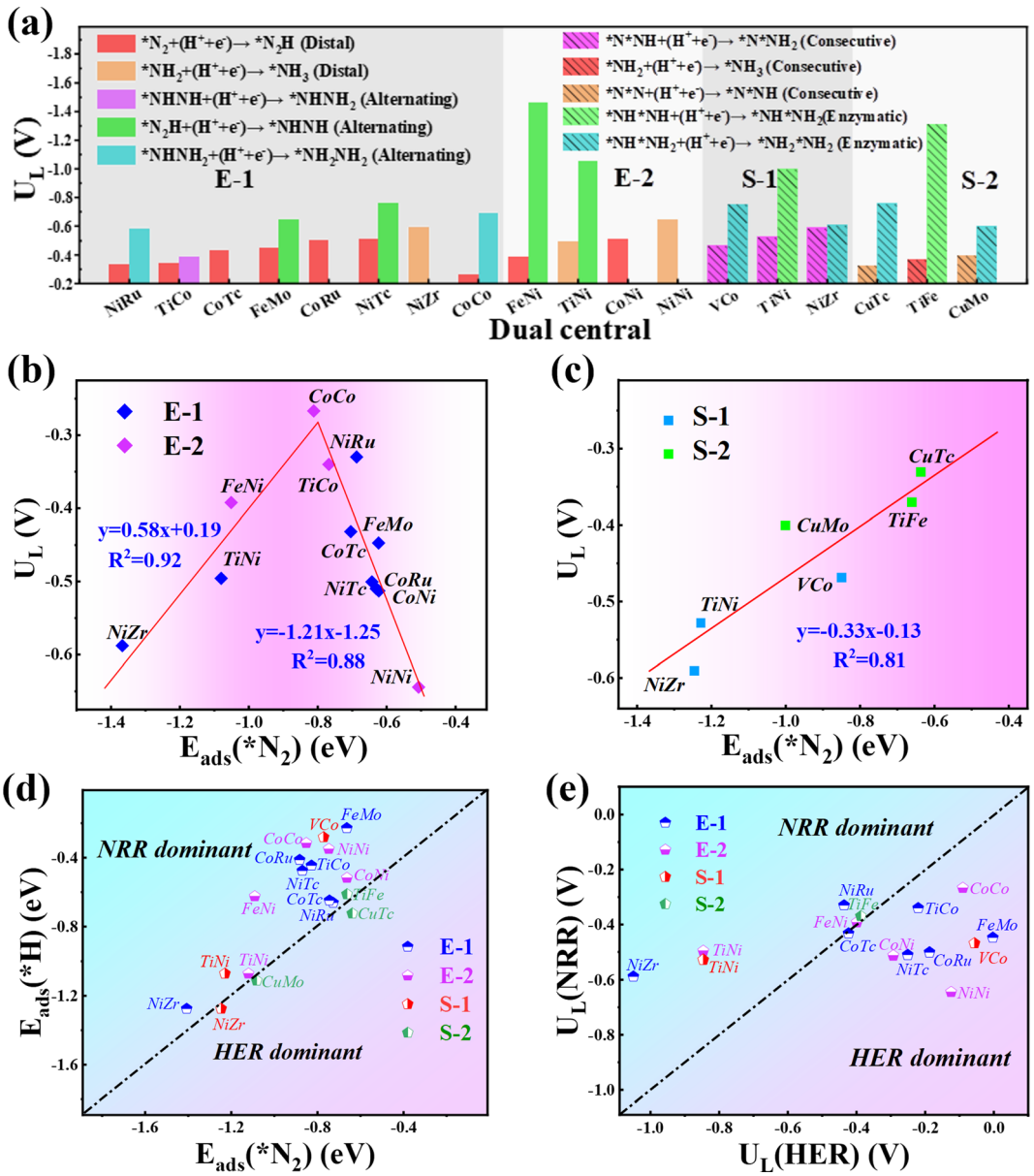


Fig. 4 (a) Theoretical limiting potentials for the NRR on the 12 and 6 promising $TM_1TM_2@C_9N_4$ candidates through the end-on configuration and side-on configuration. (b) The volcano curve between $U_L$ and $E_{ads}(*N_2)$ through (c) end-on and (d) side-on configurations. Comparison of $E_{ads}(*H)$ and $E_{ads}(*N_2)$ on 18 $TM_1TM_2@C_9N_4$ catalysts with 12 end-on configuration and 6 side-on configuration. (e) The limiting potential of the NRR ($U_L$(NRR)) and HER ($U_L$(HER)) for 15 $TM_1TM_2@C_9N_4$ catalysts with 12 end-on adsorption configuration and 3 side-on adsorption configuration.

the catalytic activity will move away from the highest activity region. For example, the $\Delta E_{ads}(*N_2)$ values of $Ni_2@C_9N_4$ and $NiZr@C_9N_4$ are −0.51 eV and −1.37 eV, corresponding to the $U_L$ of −0.64 V and −0.59 V, respectively. Similarly, a nearly linear relationship is found between $U_L$s and $\Delta E_{ads}(*N_2)$ for potentially highly active catalysts with the side-on configuration (see Fig. 4c), where $CuTc@C_9N_4$ shows optimal activity of the NRR, with $\Delta E_{ads}(*N_2)$ of −0.64 eV.

### 3.4. The NRR selectivity of $TM_1TM_2@C_9N_4$

To ensure high faradaic efficiency in the ammonia production process, it is crucial for the catalysts to overcome the challenges of competing reaction, hydrogen evolution reaction (HER), as the adsorption of H on the catalyst surface will block the active sites and cause H poisoning. Therefore, in order to determine whether the candidate catalysts are more favorable for the NRR, the higher adsorption energy of the H atom than that of the $N_2$ molecule ($E_{ads}(*H) > E_{ads}(*N_2)$) is set as the fifth screening criterion. As shown in Fig. 4d, the $E_{ads}(*H)$ values below the diagonal line are more negative than $E_{ads}(*N_2)$, indicating that H can easily cover the active site of the catalyst and inhibit the progress of the NRR. After the fifth step of screening, four candidates with side-on adsorption configurations like $V_2@C_9N_4$, $NiZr@C_9N_4$, $CuMo@C_9N_4$, and $CuTc@C_9N_4$ were eliminated. Therefore, 15 candidates with 12 end-on adsorption configurations and 3 side-on adsorption configurations remained.

To further explore the effect of the relative limiting potential ($U_L$) of the NRR and HER, the Gibbs free energy for H ($\Delta G_H$) of the remaining candidates was investigated (see Fig. S5, ESI†). Also, the $U_L$ difference between the NRR and HER ($\Delta U_L = U_L(NRR) - U_L(HER)$ was used to estimate the selectivity of the

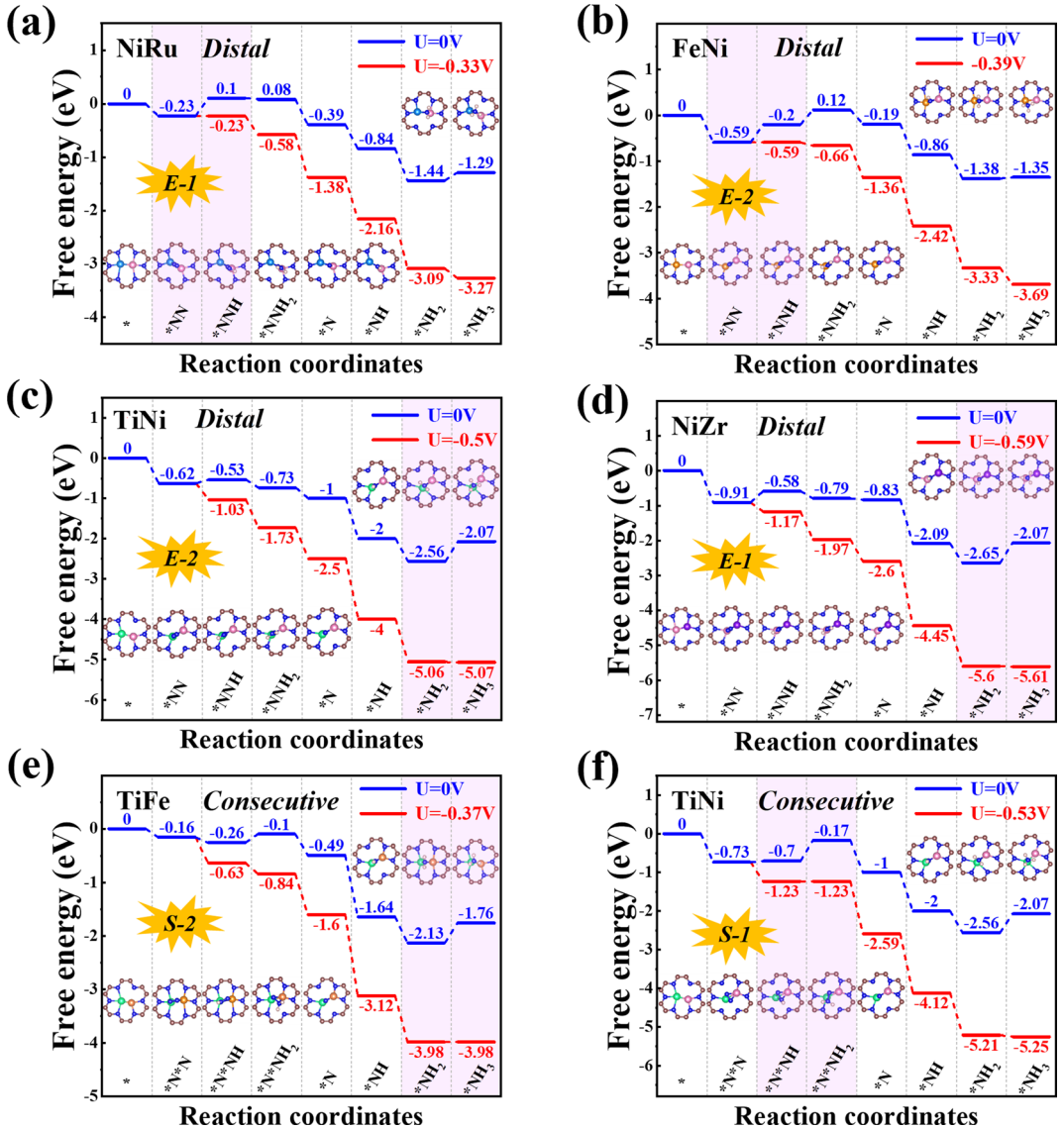


Fig. 5 Free energy diagrams of the NRR on (a) $NiRu@C_9N_4$, (b) $FeNi@C_9N_4$, (c) $TiNi@C_9N_4$ and (d) $NiZr@C_9N_4$ in the distal mechanism, (e) $TiFe@C_9N_4$ and (f) $TiNi@C_9N_4$ in the consecutive mechanism. Blue and red lines indicate free energy changes for the NRR at $U$ = 0 V and $U_L$, respectively.

 

NRR (see Fig. 4e), and $\Delta U_L > 0$ V is set as the sixth step screening criterion. Unfortunately, the most active CoCo@$C_9N_4$, which cannot guarantee a relatively positive relative limiting potential, was eliminated. After the screening, only 6 candidates with 4 end-on configurations like NiRu@$C_9N_4$, FeNi@$C_9N_4$, TiNi@$C_9N_4$, and NiZr@$C_9N_4$ and 2 side-on configurations of TiFe@$C_9N_4$ and TiNi@$C_9N_4$ remained. On the other hand, to further confirm the HER performance of these $TM_1TM_2$@$C_9N_4$ systems, we calculated the $\Delta G_H$s of 14 screened $TM_1TM_2$@$C_9N_4$ candidates (see Fig. S5, ESI†) based on third and fourth step screening criteria. Three different sites for H adsorption were considered, namely, S($TM_1$), S($TM_2$), and B(bridge) sites. The optimized structures with optimal adsorption for *H are shown in Fig. S6 (ESI†) and the hydrogen adsorption free energy diagrams ($\Delta G$(*H)) of all the candidates are shown in Fig. S7 (ESI†). Our results showed that four systems FeMo@$C_9N_4$, FeNi@$C_9N_4$, NiTc@$C_9N_4$, and CoTc@$C_9N_4$ have the optimal H adsorption site on top of the transition metal atom, while the other systems are found to have optimal H adsorption sites on the bridge site. Except FeMo@$C_9N_4$ and VCo@$C_9N_4$ that display $\Delta G$(*H), *e.g.* −0.16 eV and −0.18 eV, respectively, all the other $TM_1TM_2$@$C_9N_4$ systems showed bad HER performance with more negative $\Delta G$(*H) (< −0.2 eV).

### 3.5 NRR performance of efficient $TM_1TM_2$@$C_9N_4$

Next, we will explore the reaction mechanism and activity origin of the NRR of the six screened catalysts. Fig. 5a and d give the optimal NRR reaction pathways for NiRu@$C_9N_4$ ($U_L$ = −0.33 V), FeNi@$C_9N_4$ ($U_L$ = −0.35 V), TiNi@$C_9N_4$ ($U_L$ = −0.50 V), and NiZr@$C_9N_4$ ($U_L$ = −0.53 V) with $N_2$ adsorption through the end-on configuration. Taking NiRu@$C_9N_4$ as an example (see Fig. 5a), the reaction of adsorbed $N_2$ with hydrated protons produces an *$N_2H$ intermediate with an energy barrier of 0.33 eV. Next, H* attacks the N atom of the *$N_2H$ intermediate to form *$N_2H_2$ or *NHNH species, and H* favors the distal path due to the lower energy consumption for the formation of *$N_2H$ species. The proton–electron pair then reacts with *$NNH_2$ to release the first ammonia molecule with a free energy drop of 0.27 eV. After that, the hydrated protons then attack the remaining *N atom three times in a row, eventually releasing a second $NH_3$. Notably, the PDS of NiRu@$C_9N_4$ *via* a distal mechanism is the first hydrogenation step (*$N_2$ + *$H^+$ + $e^-$ → *$N_2H$), resulting in a $U_L$ of −0.33 V to make the whole NRR process spontaneously exothermic. A similar PDS is observed for FeNi@$C_9N_4$ (see Fig. 5b), while for TiNi@$C_9N_4$ (see Fig. 5c) and NiZr@$C_9N_4$ (see Fig. 5d), their PDSs are a remote mechanism of the last protonation step (*$NH_2$ + *$H^+$ + $e^-$ → *$NH_3$). The proton–electron pair needs to overcome a large energy barrier to attack the *$NH_2$ intermediate of N atoms; the energy barriers are 0.50 eV and 0.59 eV, respectively.

As shown in Fig. 5e and f, the optimal NRR reaction pathways for TiFe@$C_9N_4$ and TiNi@$C_9N_4$, whose $N_2$ adsorption is through the side-on configuration, are consecutive pathways. Taking TiFe@$C_9N_4$ with the S-2 adsorption configuration as an example, its second protonation of the consecutive mechanism requires only 0.16 eV, so hydrated protons tend to attack the same N atom in succession. After the first $NH_3$ was dissociated, H continued to attack the remaining N atom three times consecutively, and the last protonation step (*$NH_2$ + *$H^+$ + $e^-$ → *$NH_3$) was a PDS with an energy barrier of 0.37 eV (see Fig. 5e). Differently, the PDS of TiFe@$C_9N_4$ adsorbed by $N_2$ through the S-1 configuration is the second protonation step (*$N_2H$ + *$H^+$ + $e^-$ → *$N_2H_2$) with an energy barrier of 0.53 eV.

In order to further understand the NRR behaviors of the five screened catalysts, $TM_1TM_2$@$C_9N_4$ ($TM_1TM_2$ = NiRu, FeNi, TiNi, NiZr, and TiFe), as shown in Fig. 6b–g, the partial densities of states (PDOS) of the catalysts after $N_2$ adsorption and the crystal orbital Hamiltonian population (COHP) of the $N_2$ molecule are analyzed. The PDOS and COHP of free $N_2$ indicate that the 2π* orbital of $N_2$ gas is far from the Fermi level and is an antibonding component, revealing the strong inertness of free $N_2$ (see Fig. 6a). After $N_2$ adsorption, obvious hybridization is found for the d states of $TM_1$ and $TM_2$ atoms and the 2p state of adsorbed $N_2$ near the Fermi level for all catalysts, indicating that there is a strong bond between the catalysts and the adsorbed $N_2$, ensuring that $N_2$ can spontaneously adsorb on the active sites on the catalyst surface and being activated by the catalyst (see Fig. 6b–g). Obviously, some electron-occupied antibonding components of $N_2$ appear below the Fermi level in all the systems, which also demonstrates its activation. Taking NiRu@$C_9N_4$ as an example, the 3σ and 2π orbitals of adsorbed $N_2$ molecules donate electrons to the unoccupied d orbitals of Ni and Ru of the NiRu@$C_9N_4$ substrate, thereby enhancing the adsorption of $N_2$ molecules. In addition, the occupied d orbitals of Ni and Ru atoms donate electrons back to the 2π* antibonding orbitals of $N_2$ molecules, resulting in the separation of the 2π* antibonding orbitals into occupied and unoccupied orbitals.

In addition, the activation of the N≡N bond can also be confirmed by analyzing the integrated crystal orbital Hamilton population (ICOHP) values (see Fig. 6b–g). Our results show that the ICOHP values for $N_2$ on all the studied catalysts are negative, around −6.94 to −1.45 eV, indicating that the $N_2$ molecule is well activated. Interestingly, there is a strong linear relationship between the ICOHP value and the N≡N bond length of the adsorbed $N_2$; that is, a more negative ICOHP corresponds to a longer N≡N bond length. Similarly, such a linear relationship can also be determined between ICOHP and the charge transferred to the adsorbed $N_2$ ($\Delta Q$) (see Fig. 6i). It is noted that the more charges transferred to the $N_2$, the weaker the interaction between the N≡N bonds and the more negative the values of ICOHP.

In order to confirm the influence of the solvent effect, we chose NiRu@$C_9N_4$ and TiFe@$C_9N_4$ to perform several test calculations with and without considering the effect of solvation (see Fig. S8, ESI†). Although the free energies of the adsorbed species for both NiRu@$C_9N_4$ and TiFe@$C_9N_4$ in the distal mechanism are slightly more negative with the consideration of the solvation effect, similar energy diagrams are identified for both cases. Moreover, the differences of $U_L$ during the full NRR processes of NiRu@$C_9N_4$ and TiFe@$C_9N_4$ with and without considering the solvation effect are only −0.12 V and −0.08 V.

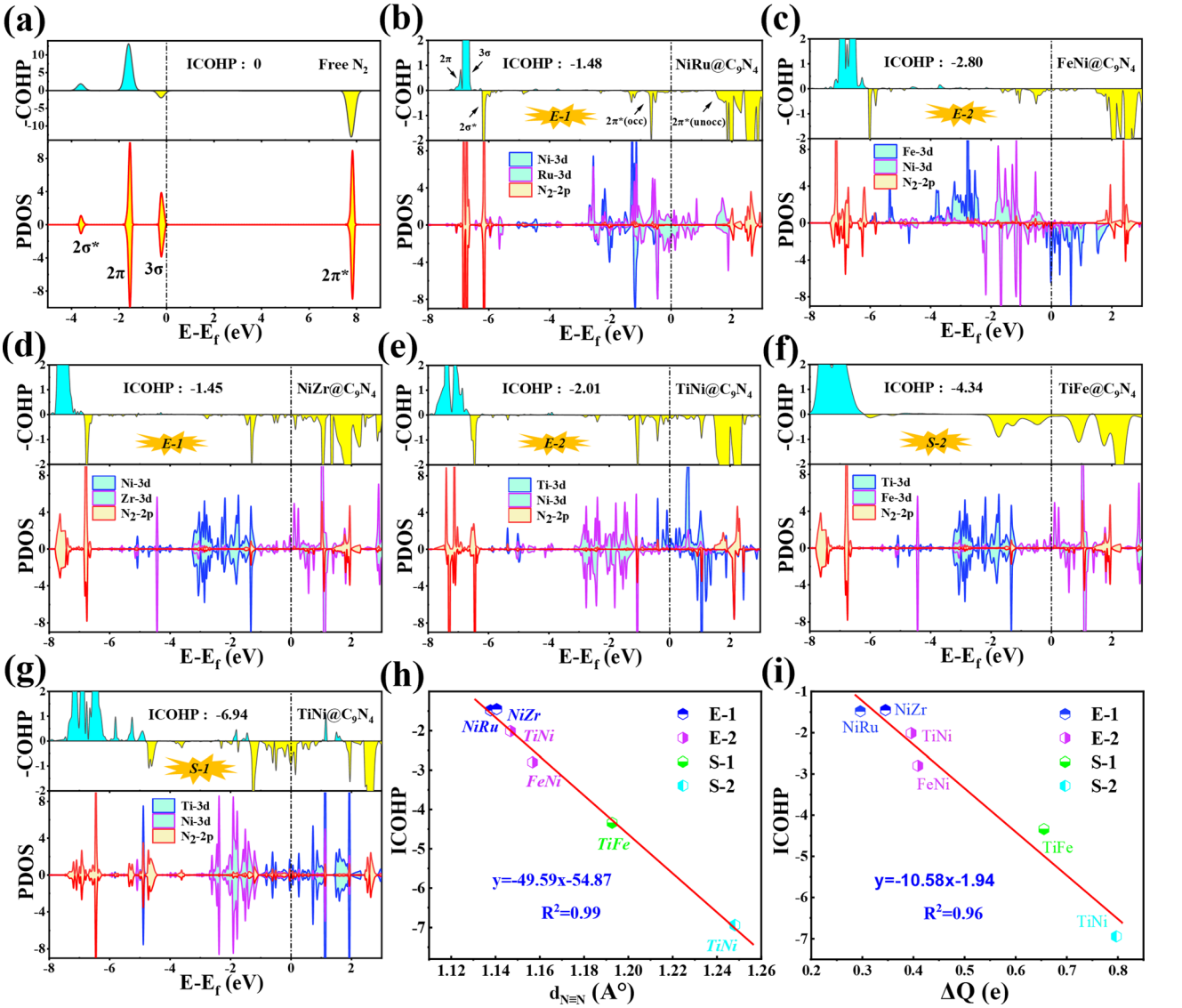


Fig. 6 (a) Partial density of states (PDOS) and molecular orbitals of a free $N_2$ molecule. (b–f) PDOS, crystal orbital Hamilton populations (COHPs), and integrated COHP (ICOHP) of $*N_2$ on NiRu@$C_9N_4$, FeNi@$C_9N_4$, TiNi@$C_9N_4$, and NiZr@$C_9N_4$ through the end-on configuration, and (g) TiFe@$C_9N_4$ and (h) TiNi@$C_9N_4$ through the side-on configuration. (h) Illustration of the correlation between ICOHP and N≡N bond length of $N_2$ ($d_{N\equiv N}$). (i) Illustration of the correlation between ICOHP and $\Delta Q$. The bonding and antibonding states in COHP are denoted by cyan and yellow, respectively.

Based on this, we can conclude that the reaction energies are not significantly affected by those solvation molecules.

### 3.6. Possibility of the experimental synthesis of $TM_1TM_2@C_9N_4$

Finally, we extended the possibility of the experimental synthesis of these screened $TM_1TM_2@C_9N_4$ catalysts. First, we calculated their formation energies using the following equation:

$$E_f = \frac{E_{TM_1TM_2@C_9N_4} - E_{C_9N_4} - E_{TM_1} - E_{TM_2}}{2} \quad (4)$$

Here, $E_{TM_1TM_2@C_9N_4}$ is the energy of monolayer $C_9N_4$ anchored with the two TM atoms, and $E_{C_9N_4}$ is the energy of monolayer $C_9N_4$. $E_{TM_1}$ and $E_{TM_2}$ represent the energies of single TM atoms in their stable bulk phase. As shown in Fig. 7a, the formation energies of $TM_1TM_2@C_9N_4$ are 0.18 eV, −0.07 eV, −0.1 eV, −0.79 eV, and −1.13 eV at $TM_1TM_2$ = NiRu, FeNi, NiZr, TiNi, and TiFe, respectively. Besides, as shown in Fig. S9–S13 (ESI†), *ab initio* molecular dynamics (AIMD) simulations of NiRu@$C_9N_4$, FeNi@$C_9N_4$, NiZr@$C_9N_4$, TiNi@$C_9N_4$, and TiFe@$C_9N_4$ are performed at a time step of 2 fs at 500 K to explore their thermal stability. Obviously, the total energy converges rapidly, and no obvious structural distortion occurs during the entire simulation time (see Fig. 7b–f), which indicates that they have relatively high thermodynamic stability, hopefully synthesized experimentally.

It is well known that the NRR active sites of catalyst basal planes can be easily covered by various functional groups under certain reaction conditions; if yes, the reaction areas in their basal planes will be largely decreased.[53,54] To address the concern whether the surfaces of the catalysts are blocked by

 

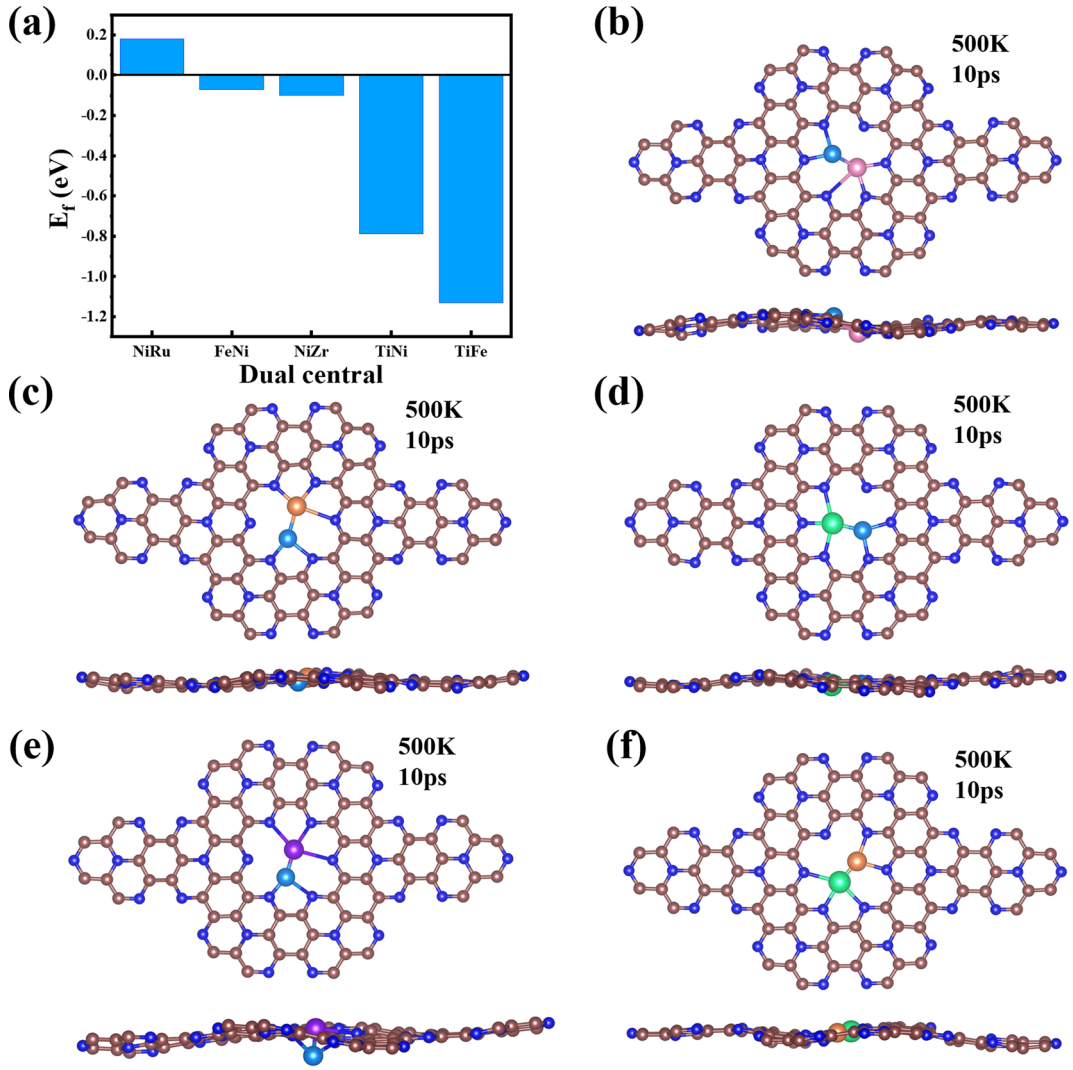


Fig. 7 (a) Formation energies of NiRu@$C_9N_4$, FeNi@$C_9N_4$, TiNi@$C_9N_4$, NiZr@$C_9N_4$, and TiFe@$C_9N_4$. (b–f) Top and side views of the configurations of NiRu@$C_9N_4$, FeNi@$C_9N_4$, TiNi@$C_9N_4$, NiZr@$C_9N_4$, and TiFe@$C_9N_4$ after AIMD simulations. The simulations were performed at 500 K for 10 ps with a time step of 2 fs.

*O/*OH like electron-accepting species or not, we constructed the surface Pourbaix diagrams of the 5 screened $TM_1TM_2$@$C_9N_4$ ($TM_1TM_2$ = NiRu, FeNi, TiNi, TiFe, and NiZr) catalysts by plotting the equilibrium potential between different surface terminations, including –O, –OH, and –$H_2O$ terminated systems, as a function of pH (see Fig. S14, ESI†). The optimal structures for *O, *OH, and *$H_2O$ adsorption are provided in Fig. S15 (ESI†). We first considered the situation with 0 V *vs.* SHE to unveil their surface composition at the cathode surface under operating conditions. Clearly, all the $TM_1TM_2$@$C_9N_4$ systems can adsorb the oxygen and hydroxyl groups onto their bare surfaces to form O*/OH*. Specifically, 3 $TM_1TM_2$@$C_9N_4$ ($TM_1TM_2$ = TiNi, TiFe, and NiZr) can be fully terminated by O*; FeNi@$C_9N_4$ can be occupied by OH*; whereas for NiRu@$C_9N_4$, both O* and OH* can be adsorbed on the basal plane depending on the pH value of the electrolyte. When an electrode potential is applied, the protonation of O*/OH* is gradually favorable on these $TM_1TM_2$@$C_9N_4$ surfaces. The redox potential ($U_R$), which is defined as the electrode potential needed to remove the surface O*/OH* species, could be compared to the $U_L$ of the NRR. Except NiZr@$C_9N_4$ with $U_R$ being higher than $U_L$, the four other $TM_1TM_2$@$C_9N_4$ systems cannot be influenced by the *O/*OH species under working conditions.

## 4. Conclusions

In conclusion, by first-principles high-throughput calculations, a 6-step screening criterion is set to identify promising candidate catalysts of $TM_1TM_2$@$C_9N_4$ for the NRR. Our calculations show that the heteronuclear dual-metal catalysts NiRu@$C_9N_4$, FeNi@$C_9N_4$, TiFe@$C_9N_4$, TiNi@$C_9N_4$, and NiZr@$C_9N_4$ are considered as promising NRR electrocatalyst candidates with good confinement potentials of −0.33 V, −0.35 V, −0.37 V, −0.50 V, and −0.59 V. In addition, we also confirmed the high selectivity and stability of these 5 catalysts. The systematic study shows

that for the $TM_1TM_2@C_9N_4$ catalyst with dual-atom active sites, the different adsorption configurations of $N_2$ have obvious differences in the origin of the catalytic activity, indicating that it is of great significance to explore the most stable adsorption configuration of $N_2$. Our findings not only provide a useful dataset for the experimental exploration of $TM_1TM_2@C_9N_4$ catalysts, but also provide a reference to guide the rational design of novel high-performance NRR catalysts for the sustainable production of ammonia.

## Conflicts of interest

There are no conflicts to declare.

## Acknowledgements

This work is supported by the NSFC (2022M711691, 22203046, and 12204404), the Open Funds of the State Key Laboratory of Rare Earth Resource Utilization (RERU2021011), and the Six talent peaks project in Jiangsu Province (XCL-104). We thank the computational resources at Yangzhou University and Hebei Normal University.

## References

1 J. Erisman, M. Sutton, J. Galloway, Z. Klimont and W. Winiwarter, *Nat. Geosci.*, 2008, **1**, 636–639.
2 J. Galloway, A. Townsend, J. Erisman, M. Bekunda, Z. Cai, J. Freney, L. Martinelli, S. Seitzinger and M. Sutton, *Science*, 2008, **320**, 889–892.
3 J. Montoya, C. Tsai, A. Vojvodic and J. Nørskov, *ChemSusChem*, 2015, **8**, 2180–2186.
4 X. Cui, C. Tang and Q. Zhang, *Adv. Energy Mater.*, 2018, **8**, 1800369.
5 X. Xue, R. Chen and C. Yan, *Nano Res.*, 2019, **12**, 1229–1249.
6 X. Guo, J. Gu, S. Lin, S. Zhang, Z. Chen and S. Huang, *J. Am. Chem. Soc.*, 2020, **142**, 5709–5721.
7 X. Liu, Y. Jiao, Y. Zheng, M. Jaroniec and S. Qiao, *J. Am. Chem. Soc.*, 2019, **14**, 9664–9672.
8 Q. Zhang, F. Meng, H. Zhong, M. Shi, Y. Zhang, J. Yan, Q. Jiang and X. Zhang, *Adv. Mater.*, 2017, **29**, 1604799.
9 J. Montoya, C. Tsai, A. Vojvodic and J. Nørskov, *ChemSusChem*, 2015, **8**, 2180–2186.
10 J. Yang, Y. Guo, R. Jiang, F. Qin, H. Zhang, W. Lu, J. Wang and J. Yu, *J. Am. Chem. Soc.*, 2018, **140**, 8497–8508.
11 H. Zhou, Y. Qu, J. Li, Z. Wang, C. Yang and Q. Jiang, *Appl. Catal., B*, 2022, **305**, 121023.
12 J. Zhao and Z. Chen, *J. Am. Chem. Soc.*, 2017, **139**, 12480–12487.
13 Y. Lin, Y. Feng, H. Zhou, Y. Han, H. Sun, L. Shi, L. Meng, M. Zhou, Y. Liu and X. Zhang, *Appl. Surf. Sci.*, 2022, **593**, 153338.
14 A. Wang, J. Li and T. Zhang, *Nat. Rev. Chem.*, 2018, **2**, 65–81.
15 L. Xu, L. Yang and E. Ganz, *ACS Appl. Mater.*, 2021, **13**, 14091–14101.
16 X. Wang, W. Wang, M. Qiao, G. Wu, W. Chen, T. Yuan, Q. Xu, M. Chen, Y. Zhang, X. Wang, J. Wang, J. Ge, X. Hong, Y. Li, Y. Wu and Y. Li, *Sci. Bull.*, 2018, **63**, 1246–1253.
17 Y. Zhang, J. Hu, C. Zhang, Y. Liu, M. Xu, Y. Xue, L. Liu and M. Leung, *J. Mater. Chem. A*, 2020, **8**, 9091.
18 Z. Geng, Y. Liu, X. Kong, P. Li, K. Li, Z. Liu, J. Du, M. Shu, R. Si and J. Zeng, *Adv. Mater.*, 2018, **30**, 1803498.
19 L. Hui, Y. Xue, H. Yu, Y. Liu, Y. Fang, C. Xing, B. Huang and Y. Li, *J. Am. Chem. Soc.*, 2019, **141**, 10677–10683.
20 Y. Wang, X. Cui, J. Zhao, G. Jia, L. Gu, Q. Zhang, L. Meng, Z. Shi, L. Zheng, C. Wang, Z. Zhang and W. Zheng, *ACS Catal.*, 2019, **9**, 336–344.
21 C. Choi, S. Back, N. Kim, J. Lim, Y. Kim and Y. Jung, *ACS Catal.*, 2018, **8**, 7517–7525.
22 H. Fei, T. Guo, Y. Xin, L. Wang, R. Liu, D. Wang, F. Liu and Z. Wu, *Appl. Catal., B*, 2022, **300**, 120733.
23 J. Yin, J. Li, Y. Hang, J. Yu, G. Tai, X. Li, Z. Zhang and W. Guo, *Small*, 2016, **12**, 2942–2968.
24 T. Yang, T. Song, J. Zhou, S. Wang, D. Chi, L. Shen, M. Yang and Y. Feng, *Nano Energy*, 2020, **68**, 104304.
25 D. Jiao, Y. Liu, Q. Cai and J. Zhao, *J. Mater. Chem. A*, 2021, **9**, 1240–1251.
26 J. Chen, H. Cao, J. Chen, S. Qian, G. Xia, Y. Wang and J. Li, *J. Phys. Chem. C*, 2021, **125**, 19821–19830.
27 Y. Le, J. Gua and W. Tian, *Chem. Commun.*, 2014, **50**, 13319–13322.
28 W. Zhao, L. Zhang, Q. Luo, Z. Hu, W. Zhang, S. Smith and J. Yang, *ACS Catal.*, 2019, **9**, 3419–3425.
29 D. Jiao, Y. Liu, Q. Cai and J. Zhao, *J. Mater. Chem. A*, 2021, **9**, 1240–1251.
30 P. Ou, X. Zhou, F. Meng, C. Chen, Y. Chen and J. Song, *Nanoscale*, 2019, **11**, 13600–13611.
31 Y. Zhang, J. Hu, C. Zhang, Y. Liu, M. Xu, Y. Xue, L. Liu and M. Leung, *J. Mater. Chem. A*, 2020, **8**, 9091–9098.
32 S. Yang, C. Zhang, D. Rao and X. Yan, *Chin. J. Catal.*, 2022, **43**, 1139–1147.
33 Y. Li, Q. Zhang, C. Li, H. Fan, W. Luo, H. Liua and S. Dou, *J. Mater. Chem. A*, 2019, **7**, 22242–22247.
34 T. Deng, C. Cen, H. Shen, S. Wang, J. Guo, S. Cai and M. Deng, *J. Phys. Chem. Lett.*, 2020, **11**, 6320–6329.
35 X. Zheng, Y. Yao, Y. Wang and Y. Liu, *Nanoscale*, 2020, **12**, 9696–9707.
36 G. Zheng, L. Li, Z. Tian, X. Zhang and L. Chen, *J. Energy Chem.*, 2021, **54**, 612–619.
37 S. Ji, Y. Chen, Q. Fu, Y. Chen, J. Dong, W. Chen, Z. Li, Y. Wang, L. Gu, W. He, C. Chen, Q. Peng, Y. Huang, X. Duan, D. Wang, C. Draxl and Y. Li, *J. Am. Chem. Soc.*, 2017, **139**, 9795–9798.
38 L. Xia, H. Wang and Y. Zhao, *J. Mater. Chem. A*, 2021, **9**, 20615–20625.
39 X. Lv, W. Wei, B. Huang, Y. Dai and T. Frauenheim, *Nano Lett.*, 2021, **21**, 1871–1878.
40 H. Chen, S. Zhang, W. Jiang, C. Zhang, H. Guo, Z. Liu, Z. Wang, F. Liu and X. Niu, *J. Mater. Chem. A*, 2018, **6**, 11252–11259.
41 Y. Zhou, G. Gao, J. Kang, W. Chu and L. Wang, *Nanoscale*, 2019, **11**, 18169–18175.
42 Z. Xue, X. Zhang, J. Qin and R. Liu, *Nano Energy*, 2021, **80**, 105527.

 

43 G. Kresse and J. Hafner, *Phys. Rev. B: Condens. Matter Mater. Phys.*, 1993, **48**, 13115.
44 G. Kresse and J. Hafner, *Phys. Rev. B: Condens. Matter Mater. Phys.*, 1993, **47**, 558.
45 G. Kresse and D. Joubert, *Phys. Rev. B: Condens. Matter Mater. Phys.*, 1999, **59**, 1758–1775.
46 J. Perdew, K. Burke and Y. Wang, *Phys. Rev. B: Condens. Matter Mater. Phys.*, 1996, **54**, 16533–16539.
47 J. Perdew, K. Burke and M. Ernzerhof, *Phys. Rev. Lett.*, 1996, **77**, 3865.
48 S. Nose, *J. Chem. Phys.*, 1984, **81**, 511–519.
49 J. Montoya, C. Tsai, A. Vojvodic and J. Nørskov, *ChemSusChem*, 2015, **8**, 2180–2186.
50 A. Peterson, F. Abild-Pedersen, F. Studt, J. Rossmeisl and J. Nørskov, *Energy Environ. Sci.*, 2010, **3**, 1311–1315.
51 P. Sabatier, Hydrogenations et deshydrogenations par catalyse, *Ber. Dtsch. Chem. Ges.*, 1911, **44**, 1984–2001.
52 X. Wang and L. Yang, *Appl. Surf. Sci.*, 2022, **576**, 151839.
53 X. Guo, S. Lin, J. Gu, S. Zhang, Z. Chen and S. Huang, *Adv. Funct. Mater.*, 2021, **31**, 2008056.
54 X. Zhu, X. Zhou, Y. Jing and Y. Li, *Nat. Commun.*, 2021, **12**, 4080.